Ultramicroscopy 215 (2020) 113007

Contents lists available at ScienceDirect

Ultramicroscopy

journal homepage: www.elsevier.com/locate/ultramic

Integrated super resolution fluorescence microscopy and transmission electron microscopy

Sajjad Mohammadian[a], Alexandra V Agronskaia[a], Gerhard A Blab[a], Elly G van Donselaar[b], Cecilia de Heus[b], Nalan Liv[b], Judith Klumperman[b], Hans C Gerritsen[a,*]

[a] Molecular Biophysics, Department of Physics, Faculty of Science, Utrecht University, Princetonplein 1, 3584 CC Utrecht, Netherlands
[b] Department of Cell Biology, Centre for Molecular Medicine, University Medical Centre Utrecht, Utrecht, Netherlands

A B S T R A C T

In correlative light and electron microscopy (CLEM), the capabilities of fluorescence microscopy (FM) and electron microscopy (EM) are united. FM combines a large field of view with high sensitivity for detecting fluorescence, which makes it an excellent tool for identifying regions of interest. EM has a much smaller field of view but offers superb resolution that allows studying cellular ultrastructure. In CLEM, the potentials of both techniques are combined but a limiting factor is the large difference in resolution between the two imaging modalities. Adding super resolution FM to CLEM reduces the resolution gap between FM and EM; it offers the possibility of identifying multiple targets within the diffraction limit and can increase correlation accuracy.

CLEM is usually carried out in two separate setups, which requires transfer of the sample. This may result in distortion and damage of the specimen, which can complicate finding back regions of interest. By integrating the two imaging modalities, such problems can be avoided.

Here, an integrated super resolution correlative microscopy approach is presented based on a wide-field super resolution FM integrated in a Transmission Electron Microscope (TEM). Switching imaging modalities is accomplished by rotation of the TEM sample holder. First imaging experiments are presented on sections of Lowicryl embedded Human Umbilical Vein Endothelial Cells labeled for Caveolin both with Protein A-Gold, and Alexa Fluor®647. TEM and FM images were overlaid using fiducial markers visible in both imaging modalities with an overlay accuracy of 28 ± 11 nm. This is close to the optical resolution of ~50 nm.

1. Introduction

In correlative light and electron microscopy, the capabilities of light microscopy (LM) and electron microscopy (EM) are combined in studies of the same sample [1]. Usually, light microscopy is carried out with a fluorescence microscope. FM has the capability of detecting specific targets with very high sensitivity and specificity in large fields of view. Imaging the same targets later with EM allows analysis of cellular content and ultrastructure with nm resolution. FM is often employed as a guiding tool for identifying regions of interest (ROIs) in large fields of view in a specimen where EM is utilized to study, e.g., the cellular matrix.

An advantage of CLEM is that it can significantly speed up the imaging of rare events in EM. In general, FM is a faster technique, fluorescence staining/labeling possibilities are broad, and labelling efficiencies are usually high. In contrast, immuno-labeling efficiencies can be comparatively low in EM, as the efficiency of primary antibody labelling in EM depends on many factors including fixation, post-fixation, and the nature of the resin. CLEM provides a unique way to unify the molecular and ultrastructure information provided by FM and EM respectively.

CLEM experiments are usually carried out using separate setups. The main advantage of this approach is that the sample can be imaged under optimized conditions for each modality. FM can be carried out using a high numerical aperture (*NA*) immersion objective and wet conditions. Wet conditions are favorable for fluorescent proteins and commonly used organic dyes. The EM heavy metal staining in the specimens can be optimized for the highest contrast. The disadvantage of this approach is that both the EM sample preparation step and the transfer of the specimen can result in distortion of the sample [2]. Moreover, when the specimen is imaged with FM using an immersion objective, traces of the immersion liquid may contaminate the specimen. Also finding back the ROI may be challenging due to the differences in dimensions, resolutions and contrast mechanisms in the FM and EM images. A few methods have been developed to overcome these challenges including the use of finder grids, microchips with SiN windows and the matching of features visible in both imaging modalities [3,4].

Integrating both imaging modalities in one setup (integrated CLEM, iCLEM) facilitates straightforward finding back the ROIs in EM. In integrated approaches, the same sample stage is used for both FM and EM. This results in a straightforward and fast "coarse" correlation

* Corresponding author
E-mail address: H.C.Gerritsen@uu.nl (H.C. Gerritsen).

https://doi.org/10.1016/j.ultramic.2020.113007
Received 7 January 2020; Received in revised form 14 April 2020; Accepted 19 April 2020
Available online 06 May 2020

between the FM and EM images. In the integrated CLEM system presented here, for instance, switching imaging modalities only requires rotation of the TEM specimen holder. This can be carried out in seconds and the initial correlation accuracy between FM and EM images is already within 1 μm. Avoiding specimen distortion and damage is straightforward in integrated CLEM systems. In our experience the integrated approach is more robust and has a higher success rate than non-integrated approaches. We note that the integrated approach is particularly advantageous for cryo applications where contamination of the specimen can be a serious threat [5]. Furthermore, integrated CLEM systems are very promising for automated high-throughput CLEM studies.

A distinct disadvantage of integrated CLEM approaches is that the sample needs to be compatible with both FM and EM. This can be challenging for room temperature applications. One of the main issues is that the heavy metals used in EM sample preparations quench fluorescence. Furthermore, many fluorescent probes do not perform well under dry/vacuum conditions [6,7]. A number of protocols have been introduced both for TEM and SEM sample preparation that mitigate these problems [6–10]. Integrated CLEM has seen rapid developments over more than a decade and several commercial iCLEM systems are currently available [11–14]. Previously, we developed an integrated CLEM based on a laser scanning microscope module that is mounted on a side port of a TEM column (the iLEM, [11]).

In CLEM approaches based on wide-field and confocal fluorescence microscopy techniques, there is a large resolution gap between the EM and FM imaging modalities. Diffraction effects limit the optical resolution to a few hundred nm. Developments in super resolution FM (SR-FM) pushed the limit of optical microscopy to several tens of nanometers [15]. SR-FM decreases the resolution gap between FM and EM and several examples exist of CLEM based on SR-FM [16–19]. The high fluorescence labeling efficiency and the sensitivity of FM in combination with SR-CLEM offers the potential of mapping the fluorescence of single fluorescently labeled molecules on top of EM images with an accuracy of several tens of nanometers. In SR-CLEM minimizing distortion of the specimen between imaging steps is even more important than in conventional CLEM. Integrating SR-FM and EM is a straightforward way to accomplish this.

Recently, it was shown that the overlay accuracy and resolution power of SR-FM allows skipping EM labeling in an integrated SR-FM/SEM system [20]. However, here the partial water vapor pressure had to be increased to 2 mbar by injecting water vapor into the SEM to make the fluorophore (Green Fluorescent Protein, GFP) blink and record SR images. This is comparatively easy to accomplish in a SEM but not realistic in a TEM because of the required high vacuum pressure $\sim 10^{-6}$ mbar. In our work, we demonstrate that SR-FM can be realized inside a TEM using Alexa Fluor®647, a conventional fluorophore.

This manuscript describes the integration of a home-made SR-FM microscope into a TEM column. Design considerations, including the choice of SR technique, and the performance of the system are discussed. Finally, the integrated SR-CLEM setup was used for the imaging of Lowicryl sections of Human Umbilical Vein Endothelial Cells (HUVECs) labeled for Caveolin, with Protein A Gold, and Alexa Fluor®647. In these experiments, a super resolution of ~50 nm was realized and the overlay accuracy of SR-FM and TEM images was about 28 nm. We note that continuous structures like actin filaments and microtubules are commonly used for testing the image fidelity in SR microscopy. However, this is not an option here. TEM samples are typically very thin (~70 nm in our case) and continuous structures will not be confined to a single thin section.

2. Materials and methods

2.1. Super resolution module

2.1.1. Super resolution method

SR-FM can be carried out in a number of different ways. Several of the existing SR methods are incompatible with integration in TEM. Implementation based on Stimulated Emission Depletion [21] and Saturated Structured Illumination Microscopy (SSIM, [22–24]) require very high laser powers which can easily damage the thin sample [15,25]. In addition, they require very accurate alignment of the optical beams, which complicates practical implementations. Some of the localization based SR methods are promising candidates for integration in TEM. Localization based SR microscopy relies on pinpointing the position of the fluorescence signal of single molecules, which can be done with a precision of several tens of nanometers [26–31]. The switching between a fluorescent and a non-fluorescent state helps to prove that a molecule is spatially isolated. In the case of a single molecule signal, switching between two signal levels is observed while events involving multiple molecules yield more and higher signal levels. The speed of the switching between the dark and fluorescent states depends on many details including the SR technique employed, properties of the fluorescent dye, experimental condition etc. For the analyses of the images (movies) software is used that rejects false events. Important elements in the rejection filter are the size of the light spots and the brightness of the spot. The spots should be approximately of the size of the diffraction limit. The signal strengths of single molecules are about equal; too high signals are due to the presence of multiple molecules in the spot and too low signals may be caused by background fluctuations.

Localization based methods like Stochastic Optical Reconstruction Microscopy (STORM, [26]), direct STORM (dSTORM, [27]) and Ground State Depletion microscopy followed by Individual Molecule return (GSDIM, [28]) highly depend on the surrounding environment or buffer medium to keep the fluorophore in a long lived dark state [29] or to switch fluorophores on and off. These conditions are not compatible with the dry/vacuum conditions inside the TEM.

In Photo Activated Localization Microscopy (PALM, [30,31]), fluorescent molecules are converted from a dark state to a fluorescent state by illumination with a laser. PALM does not require special media and shows only comparatively little dependency on the environment [29]. In addition to PALM, localization microscopy of randomly blinking dyes which don't depend on the presence of oxygen for blinking [32,33] has prospects to work in integrated systems. Our design includes possibilities to employ both PALM and spontaneously blinking fluorescent dyes. For, localization based SR microscopy the precise mechanism of the on/off switching is not relevant. The validation experiments described here rely on the spontaneous on/off switching of Alexa Fluor®647, a commonly used fluorophore.

2.1.2. Design considerations

The integrated SR microscope was designed and manufactured in house. For integrating the SR microscope into the TEM column a similar strategy as with the iLEM [11] was followed. The SR module was mounted at one of the side ports of the TEM column. To switch between SR imaging mode (Fig. 1a) and TEM mode (Fig. 1b), the sample holder is rotated over 90°. The space inside the TEM column is very limited and restricts the choice of the objective. In the iLEM a simple miniaturized objective lens was used that could be positioned between the poles of the TEM very close to the specimen. Such objectives, however, are not very well optically corrected and show significant levels of aberration. Here, we opted for using a commercial long working distance microscope objective. Such objectives are well corrected for different types of optical aberrations but are comparatively large. Due to constraints imposed by the TEM poles, the maximum cone angle that fits between the pole pieces is 35°, which corresponds to an *NA* of 0.57 (Fig. 1a green dashed cone).

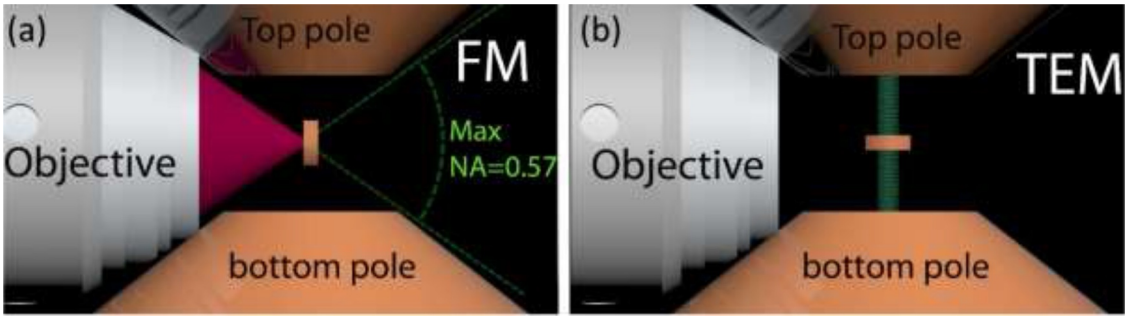

Fig. 1. Diagram showing microscope objective, sample and TEM poles. (a) Orientation of sample holder for SR measurement and (b) for TEM measurements.

In super resolution localization microscopy, the resolution is determined by the accuracy with which the location of a fluorophore can be estimated. Each fluorophore acts as a point source of light and its 2D diffraction limited wide-field microscopic image has the shape of an Airy pattern:

$$A(r) = I_0\left[2\frac{J_1\left(\frac{2\pi}{\lambda}NA\ r\right)}{\frac{2\pi}{\lambda}NA\ r}\right]^2 \quad (1)$$

Where I_0 is the peak intensity, J_1 is the first order Bessel function of the first kind, λ is the emission wavelength, and r is the radius from the center of the peak. The shape of the diffraction limited spot is often approximated by a Gaussian function to speed up the calculation of the super resolution images [34]:

$$G(r) = I_0\exp\left(-\frac{r^2}{2s^2}\right) \quad (2)$$

Here, s is the standard deviation of the fitted Gaussian. Combining eqs. (1) and (2) results in an expression for s in terms of NA and λ [34]:

$$s = 0.22\frac{\lambda}{NA} \quad (3)$$

The relation between the Full Width Half Maximum (FWHM) of the fit and s is given by Eq. 4.

$$FWHM = 2\sqrt{2ln2}\ s \approx 2.355\ s \quad (4)$$

The Gaussian fits of each spot provide the center of the peaks with a certain precisionσ. This precision, the localization accuracy, can be approximated [35] by:

$$\sigma = \sqrt{\left(\frac{s^2 + a^2/12}{N}\right)\left(1 + 4\tau + \sqrt{\frac{2\tau}{1+4\tau}}\right)} \quad (5)$$

Here $\tau = 2\pi b^2(s^2 + a^2/12)/Na^2$ where N is the number of detected photons, a the pixel size in the object plane, and b the standard deviation of the background signal (including both background fluorescence emission and detector noise). The pixel size in the object plane (a) should be approximately equal or slightly bigger than s.

In standard SR applications high NA oil (1.4–1.49) or water (1.33) immersion objectives are used. These objectives offer high spatial resolution and high collection efficiency. In our case, a commercial microscope objective with NA 0.55 is used. To evaluate the effect of the comparatively low NA on performance we compared the localization accuracy of this objective with objectives commonly used in SR imaging. Localization accuracies (σ) were calculated using MATLAB for a wavelength of 650 nm using Eq. 5 and $a \simeq 1.19\ s$. The localization accuracy was calculated for different numbers of detected photons N and background standard deviation b for an event, and is depicted in the contour plots Fig. 2a (NA = 1.4, oil, s = 97 nm), Fig. 2b (NA = 1.2, water, s = 125 nm) and Fig. 2c (NA = 0.55, air, s = 247 nm). Using the high NA oil objective, a resolution better than 25 nm can be obtained for background standard deviation levels of ~20 photons and a few hundred detected photons. To realize a similar accuracy with the low NA air objective (Fig. 2c) the background standard deviations needs to be decreased and/or the number of detected photons increased.

Out-of-focus fluorescence can significantly contribute to the background standard deviation. Interestingly, in the case of ultra-thin specimens like TEM sections (~70 nm) the volume that contributes to the background is very low. The number of detected photons depends on the number of photons emitted by the fluorophore, the collection efficiency of the objective and the efficiency of the rest of the microscope detection path and the detector.

The NA of the objective is an important factor in the collection efficiency of the objective. This efficiency does not depend on the index of refraction (n); if we consider isotropically emitted fluorescence, it only depends on the angular aperture of the microscope objective (θ in Eq. 6).

$$NA = n\ Sin(\theta) \quad (6)$$

The collection efficiency of the objective is given by:

$$Eff_{col} = \frac{1}{2}(1 - \cos(\theta)) \quad (7)$$

Using Eq. 7, the collection efficiencies are found to be 8% for the *0.55NA* air objective, 31% for the *1.4NA* oil immersion objective and 28% for the *1.2NA* water immersion objective. The detection efficiency of the *0.55NA* objective is about 4 times worse than of the *1.4NA* objective. Fig. 2c shows that this is enough for SR imaging, in particular when bright fluorophores are used, and background is minimized.

2.1.3. Implementation of the SR module

The SR module was equipped with a long working distance commercial microscope objective with a working distance of 8.7 mm and an NA of 0.55 (Nikon bright field 50X, CF IC EPI Plan ELWD). The NA of the objective was close to the maximum NA allowed by the pole shoes of the TEM, but the physical dimensions of the objective body were slightly too large. Therefore, part of the tip of the objective was milled away to get close enough to the specimen (Fig. 3). In addition, to prevent charging of the objective front lens, a conductive Indium Tin Oxide (ITO) layer was deposited on the surface of the front lens by Physical Vapor Deposition (VDL Enabling Technologies Group, Eindhoven, the Netherlands). From the wavelength dependency of the transmission of the objective, a thickness of the deposited ITO coating of around 200 nm was estimated [36,37].

A 50 μm insulating Kapton film was placed between the objective and the TEM poles to avoid electrical contact. Tests revealed that the optical performance of the objective was not affected by the TEM vacuum or removal of part of the objective housing. Importantly, no increase of the vacuum pressure was observed.

The optical layout of the fluorescence microscope module is shown in Fig. 4a. The microscope was equipped with three lasers mounted in a LightHUB® Compact Laser Combiner (Omicron-Laserage Laserprodukte GmbH). The setup was equipped with a 405 nm diode laser with 120 mW maximum output power (LuxX® 405-120) for photoactivation

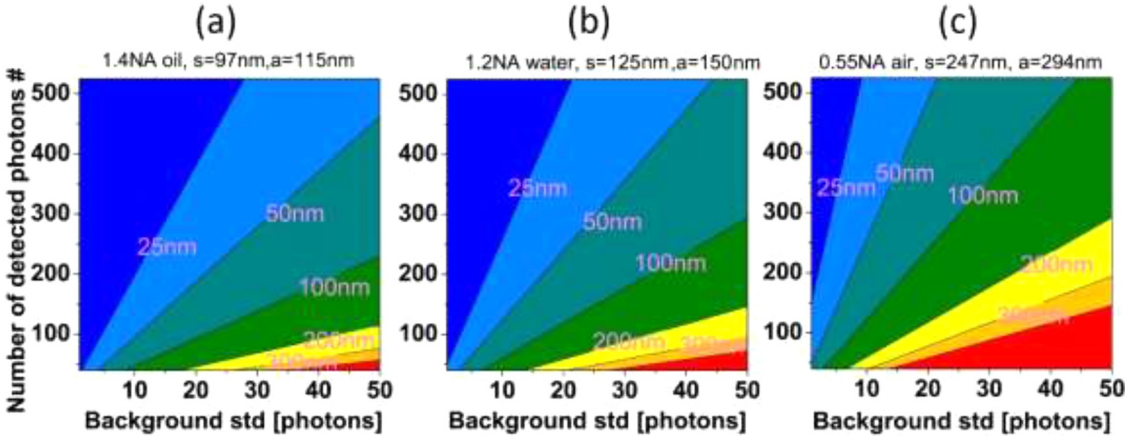

Fig. 2. Contour plots showing the localization accuracy of different objectives for different numbers of detected photons and different background standard deviations. (a) 1.4NA oil immersion objective, (b) 1.2NA water objective, (c) 0.55NA air objective.

(not used in this work). In addition, a 633 nm diode laser with 100 mW maximum power (LuxX+® 633-100) and a 532 nm solid-state laser (Cobolt Samba™) with 100 mW maximum power were available to excite fluorophores. The output power and modulation of the latter solid-state laser was controlled via an acousto-optic modulator, while the outputs of the other two lasers were controlled electrically. The outputs of all three lasers were coupled into the same single mode, polarization-maintaining fiber that guides the laser light to the microscope module. The light coming out of the fiber first passed through a collimator lens to create a parallel beam of light and next through a λ/4 waveplate to produce circularly polarized light.

After passing through a removable beam expander (L1 and L2 in Fig. 4a), the laser light was focused by a lens (L3) at the back aperture of the *0.55NA* air objective. In between L3 and the objective a dual-band dichroic mirror (Semrock, 545/650 nm BrightLine® dual-edge dichroic beam splitter) was positioned that reflected the laser light and transmitted the fluorescence emission.

Fluorescence from the specimen was collected by the objective, send through the dichroic mirror and filtered by either a long pass emission filter (Semrock, BrightLine BLP01-635R) or a multiband emission filter (Chroma, ZET532/640m) sitting in a motorized filter wheel with 4 positions. Finally, the fluorescence was recorded using a low noise, high quantum efficiency sCMOS camera (PCO AG, pco.edge 4.2). It had pixels of size 6.5 μm x 6.5 μm and one analog-to-digital conversion unit corresponds to 0.46 electrons. In addition, it was comparatively small and light (~700 g). The magnification of the objective lens was

Fig. 3. Photographs showing the objective. Part of the objective is milled away to make it fit close enough to the specimen. The right photograph shows the objective mounted on a TEM octagon.

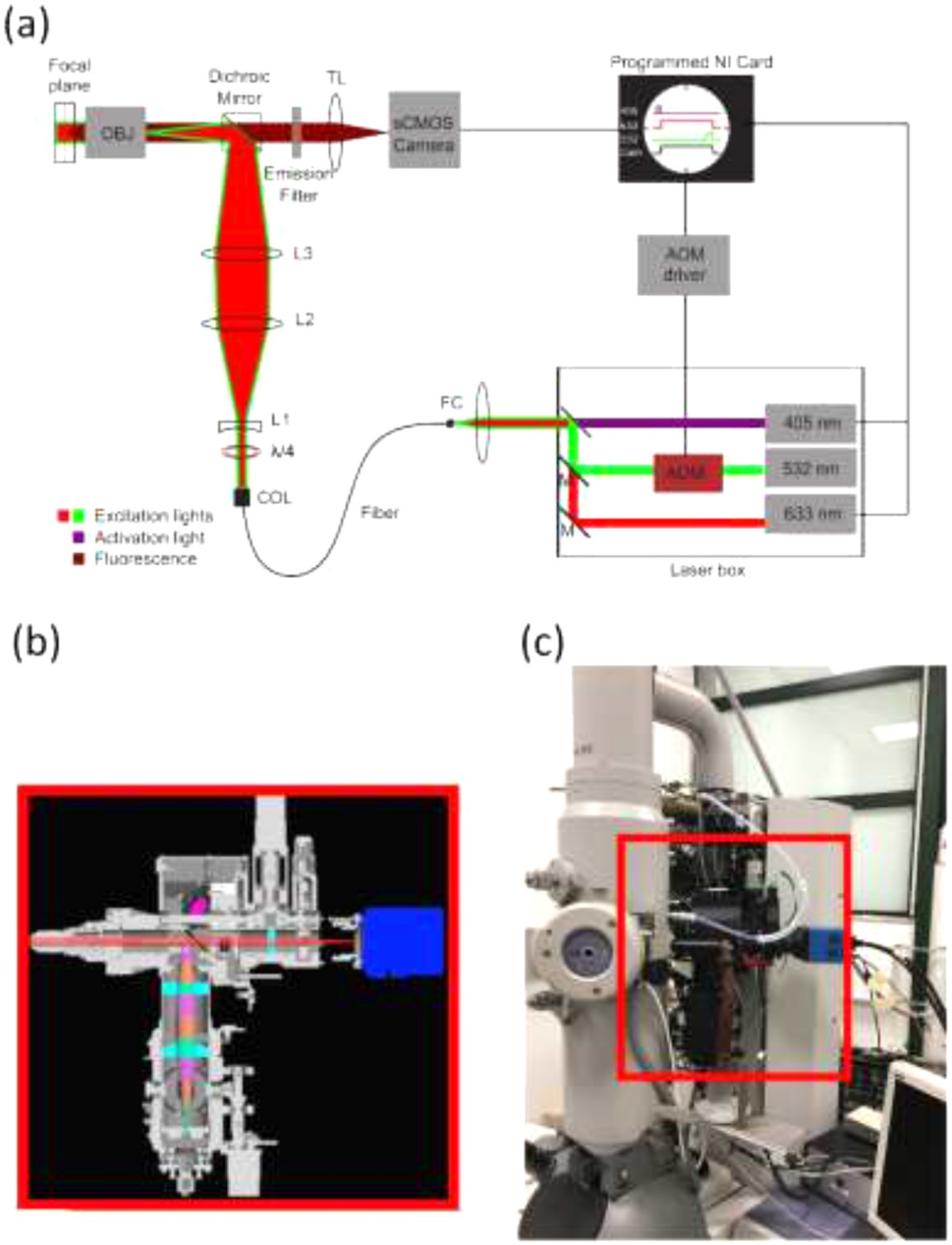

Fig. 4. The SR module. (a) Diagram of the optical design of the module. (b) CAD drawing of the module including the optical paths. (c) Photograph of the mounted module.

specified to be 50x. However, here a tube lens (TL in Fig. 4a) with a focal length of 100 mm was used, which resulted in a total magnification of 24.8x. Therefore, one pixel of the camera corresponded to 262 nm in the object plane. X-rays produced during TEM measurements are potentially damaging to the camera and harmful to the users. Therefore, one position of the filter wheel was equipped with a lead slab to stop X-rays. Another position was empty to allow recording of reflection images from the specimen. The remaining positions contained emission filters for fluorescence imaging.

The microscope could operate at two different fields of view. A large field of view (FOV) of ~400 × 400 μm^2 for searching and identifying regions of interest and a smaller field of view of ~40 × 40 μm^2 for SR imaging. The latter required high excitation powers (kWs/cm^2) which was realized by (motorized) removal of the 10x beam expander from the excitation beam path. This concentrated the available power on a smaller region.

To control and synchronize different laser illumination patterns and camera exposure times, a National Instrument card (NI PCIe-6259, National Instruments Corp.) was used. The whole system was controlled using homemade software written in LabView (LabView, National Instruments Corp.).

Fig. 4b shows a CAD drawing of the design including the optical paths and Fig. 4c shows a photograph of the module installed on a side port of the TEM. The reproducibility of the sample holder position when switching between SR-FM and TEM mode amounts to ~1 μm. This is sufficient for a first coarse correlation between SR-FM and EM images without the use of, for instance, finder grids.

2.2. Sample

2.2.1. Biological sample preparation considerations

In the case of correlative microscopy based on separate fluorescence and electron microscopes, the sample is first imaged using FM and after preparation for EM the sample is transferred to the EM. To obtain good

EM contrast, samples are usually stained with heavy metals which mostly quench the fluorescence [9,38]. In integrated microscopes, the sample is imaged inside the same system without removing the sample for additional treatment. Therefore, a single sample preparation procedure is required that is compatible with both FM and TEM. Importantly, the sample preparation should not quench the fluorescence and the fluorescent dyes should perform well under the dry, vacuum conditions. Karreman et al. introduced a preparation method for both Lowicryl [6] and Tokuyasu cryo-sections [8] that can be used for integrated systems. The SR-iCLEM experiments in this work were carried out on Lowicryl embedded sections without any post-staining with heavy metals.

The high vacuum conditions inside the TEM restricts the number of usable fluorescent dyes. Only dyes that perform well under dry, oxygen free conditions can be used. It has been shown by Karreman et al. [6,8] that Cy2 and TRITC perform reasonably well under these conditions. However, in addition to vacuum compatibility, localization based SR microscopy requires the use of dyes that show intermittent emission.

It was demonstrated that GFP-C1 and YFP-A3 exhibit blinking in the presence of water vapor (pressure ~200 Pa) in an integrated system, but are completely dark under the normal SEM vacuum conditions [7,20]. This renders these fluorescent proteins unusable for application in the high vacuum of a TEM. Another complication that further restricts the number of usable fluorophores is that dyes like Alexa Fluor®488, Atto 488, Alexa Fluor®555 and Alexa Fluor®568 require the presence of oxygen for blinking [32,33].

In the example presented here, Alexa Fluor®647 is used. This is a photoactivatable cyanine-based dye that combines a short duty-cycle with a large number of photons emitted per switching cycle (photon budget). Here, duty-cycle is the fraction of the time a fluorophore spends in the “on” state; this is inversely proportional to the number of localizable fluorophores in a diffraction-limited region. The photon budget limits the resolution in localization based SR microscopy. Alexa Fluor®647 has been shown to blink in the absence of oxygen [32,33]. Moreover, Alexa Fluor®647 is an excellent red-absorbing dye; red excitation light in general results in low background fluorescence.

2.2.2. TEM grid preparation

Different types of supporting films on top of TEM grids were tested to identify films with the lowest amount of background fluorescence that can tolerate the laser intensities used here. Polystyrene film was found to perform best (data not shown). TEM grids (200 mesh hexagonal copper grids, Stork-Veco b.v.) were coated with Polystyrene according to the method described by M. A. Hayat [39]. To make the grids sticky for the Polystyrene film, the grids were pre-treated with a 0.15% Butvar solution in Chloroform. The Butvar treated grids were gently pressed with the sticky side onto the Polystyrene film until visible lines in the Polystyrene film appeared.

2.2.3. Sample preparation for integrated SR and TEM

Preparation, fixation, freeze substitution, and Lowicryl HM20 embedding of HUVECs were previously described elsewhere [40]. Ultrathin sections (70 nm) of the embedded HUVECs were collected on Polystyrene coated TEM grids. Sections were then blocked by 1 % Bovine Serum Albumin (BSA) in PHEM, and labeled for Caveolin (Rabbit anti-Caveolin, diluted 1:300, BD Biosciences), with Protein A Gold (PAG, Cell Microscopy Center, UMC Utrecht, the Netherlands), and Alexa Fluor®647 (Chicken anti-Rabbit, diluted 1:250, Invitrogen). Next, grids with sections were washed five times in PHEM buffer and five times in water and placed in an open grid box in the dark to dry. Dried grids were sandwiched between two coverslips and the space between section and cover glass filled with 20% Glycerol. To verify the labeling step, the grids were imaged using a Deltavision RT wide-field microscope equipped with an Olympus 100X-1.40 *NA*-UPLSApo/O oil objective. After imaging, the samples were rinsed with water and dried in air.

We note that although the Protein A Gold and Alexa Fluor®647 labelling both target Caveolin, they will in general not reside on the exact same Caveolin molecule. However, they will reside on the same Caveolae if they are within the right distance (~50 nm, the typical size of Caveola).

Before transfer of a grid to the integrated microscope fiducial markers, 0.1 μm diameter TetraSpeck™ microspheres were put on top of it. To do so, the stock solution of TetraSpeck™ was diluted 1:50 in Milli-Q water. Next, the grid was incubated for 10 min on a 25 μl droplet of the solution with the fiducial markers on parafilm. Here, the side of the grid containing the section was facing the droplet. After washing the grid 3 times for 10 s in 100 mL beakers filled with Milli-Q water, excessive water was removed with filter paper. Finally, the grids were held in cross-over forceps to dry.

2.2.4. Preparation of stage calibration sample

The sample used for calibrating the sample stage was prepared by putting 0.1 μm diameter TetraSpeck™ microspheres on grids containing Lowicryl sections. The procedure was similar to the biological sample preparation the only difference being that the sections were not labeled with fluorescent dye or gold.

2.2.5. TEM reference sample

A “Plane spacing 0.9 nm and 0.45 nm, Crocidolite crystal, 3.05 mm grid” was purchased from Agar Scientific (AGS122) and used without further treatment for examining the resolution of the TEM after integration of the optical module.

2.3. Imaging

2.3.1. Super Resolution imaging

In the SR imaging experiments an area of 40 × 40 μm^2 was imaged with each camera pixel corresponding to 262 nm in the specimen. The specimen was excited at 633 nm with a continuous excitation power of 1.8 kW/cm^2. This caused spontaneous blinking of the Alexa Fluor®647 with sufficient signal for localization based SR imaging. The emission of the TetraSpeck fiducial markers is considerably dimmer than the Alexa Fluor®647. Therefore, the 532 nm diode laser was used to continuously excite the sample (350 W/cm^2) and increase the brightness of the fiducials. The camera acquired fluorescence images in free running mode with an exposure time of 100 ms and no delay between acquisitions. The total acquisition time for one SR image based on 10176 frames was about 17 min. Frames 1-10046 were recorded with both lasers switched on and contained the signals from both Alexa Fluor®647 and the TetraSpeck fiducials. This series was used to calculate the SR-image and for a drift correction based on the positions of the TetraSpeck fiducials. The remaining frames (frames 10047–10176) were recorded with only the 532 nm laser switched on. These frames only contained emission of the TetraSpeck microspheres and were utilized for accurate overlaying of the SR-FM and TEM images.

2.3.2. TEM

A modified Tecnai 12 (FEI Company) equipped with a TWIN lens was used for TEM. The sample stage of the TEM was modified to allow tilt angles from +90 to -70^0. For TEM of biological samples the acceleration voltage was set to 80 kV whereas for imaging of TEM reference samples the acceleration voltage was 120 kV. Images were acquired at room temperature using a TEMCam-F214 CCD camera (2048 × 2048 pixels; TVIPS, Gauting, Germany) with an integration time of 1 s.

2.4. Image analysis

2.4.1. SR image analysis

To analyze the SR images, the ThunderSTORM plugin for ImageJ was used [41]. The results were drift corrected using fiducial markers

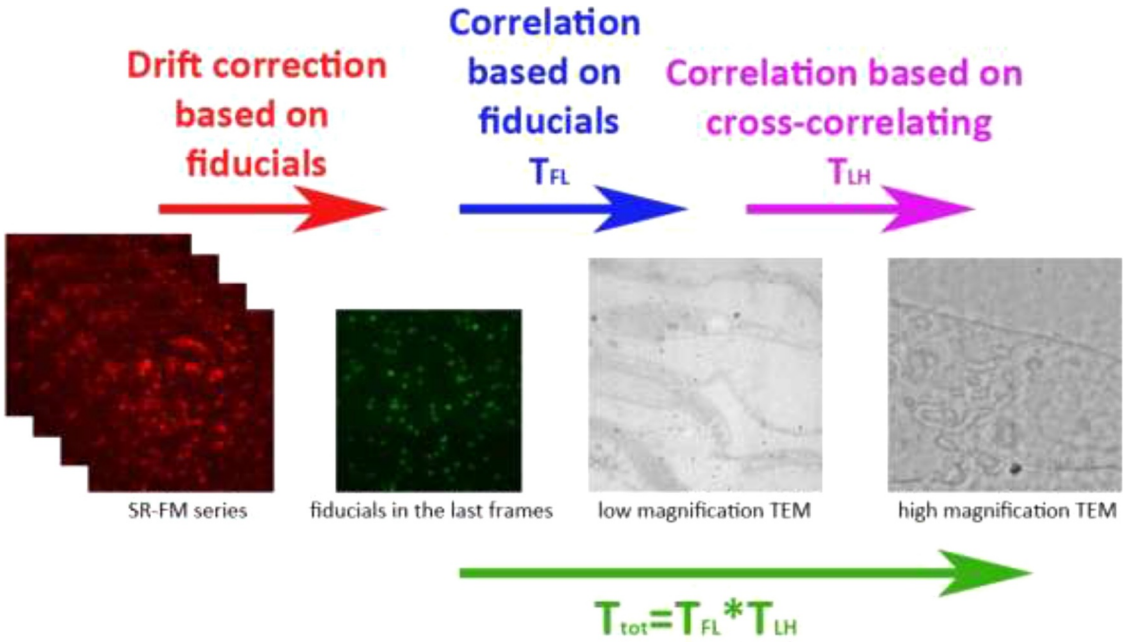

Fig. 5. Steps in correlating SR-FM with high magnification TEM images.

and only events with a fitted FWHM between 470 nm and 825 nm were used to construct the super resolution image. The lower limit of 470 nm is well below the diffraction limited FWHM of 630 nm and serves to reject noise. The higher limit supports the rejection of clusters of multiple fluorophores. The SR images overlaid with the High magnification TEM images were further thresholded by removing events with an uncertainty above 40 nm.

2.4.2. Region of interest retrieval

The use of the same sample stage for FM and TEM in our integrated CLEM system offers a simple and fast coarse correlation between FM and TEM images. Switching imaging modes only involves rotating the TEM sample holder. This sample holder determines the accuracy of the coarse correlation. By recording the reproducibility of the positions of the same fiducial markers in both imaging modalities, this accuracy was found to be about 1 μm. Consequently, ROIs identified by FM can be easily found back in TEM.

2.4.3. Overlaying images

The procedure to correlate (SR) FM and high magnification TEM images is depicted in Fig. 5 and was carried out using MATLAB. There are three steps involved; first, the images are corrected for stage drift. Next, the transformation matrix (T_{FL}) is calculated between the positions of a set of fiducial markers in FM and low magnification TEM images. Finally, the transformation matrix (T_{LH}) between low magnification and high magnification TEM images is determined using cross-correlation. Sample shrinkage occurring after the recording of the low magnification TEM image is corrected for in this cross-correlation step. Multiplying these two matrices produces the total transformation matrix (T_{tot}) between the FM and high magnification TEM images. The detailed procedure for determining T_{FL} and T_{LH} is described elsewhere [42].

To map the (regular) FM images onto the high magnification TEM images the sum of a number of FM frames was calculated and transformed using the transformation matrix (T_{tot}). The same transformation matrix was applied to the coordinates of the SR events found by the ThunderSTORM software. The transformed SR coordinates were represented by 3 × 3 pixel squares in the overlaid images. The color-coded intensity is proportional to the event's localization uncertainty. A color bar was added to indicate the localization uncertainty of the events. Bright colors depict events with low localization uncertainty and dark colors relate to high uncertainties.

3. Results

3.1. TEM performance

To test the performance of the TEM after incorporation of the optical module in the TEM column an asbestos crystal sample was imaged (Fig. S2 in supporting information (SI)). The crystal has two spacings, 0.90 nm along the crocidolite fiber (020) and 0.45 nm at a 60° angle with respect to the other axis (021). Imaging this sample at 120 kV and a magnification of 350 K clearly revealed the sub-nanometer features of the test sample. The resolution of the TEM was not significantly affected by the optical module.

3.2. SR-CLEM

The integrated SR-CLEM setup was validated by the imaging of Lowicryl sections with HUVECs labeled for Caveolin with both Protein A Gold, and Alexa Fluor®647.

The Alexa Fluor®647 dye exhibits spontaneous blinking during excitation at 633 nm (see Movie S1 in SI). For correlating the SR-FM and TEM images, TetraSpeck microspheres were used as fiducial markers. Fig. 6a shows the sum of the first 100 frames of the FM time series in red (excitation at 633 nm), overlaid with an image of the TetraSpeck fiducial markers in green (excitation at 532 nm). The fiducials were also visible during the recording of the FM time series, but their intensities were dim compared to the bright Alexa Fluor®647 intensities due to the use of the 633 nm excitation wavelength. Yellow spots in the figure correspond to positions with both a fiducial marker and Alexa Fluor®647. The white arrows in Fig. 6a point at fiducial markers that are visible in both the SR-FM and the low magnification TEM image. The fiducial markers were used to correct the time series of FM images for stage drift. In Fig. 6b, a SR image is shown that was calculated from the full time series. The color of the spots in the SR image corresponds to the localization uncertainty for the events (in nm).

After the recording of the SR-FM image, the corresponding region was imaged in the TEM. A low magnification TEM image was recorded of the 24 × 24 μm^2 region indicated by the white square in Fig. 6a and

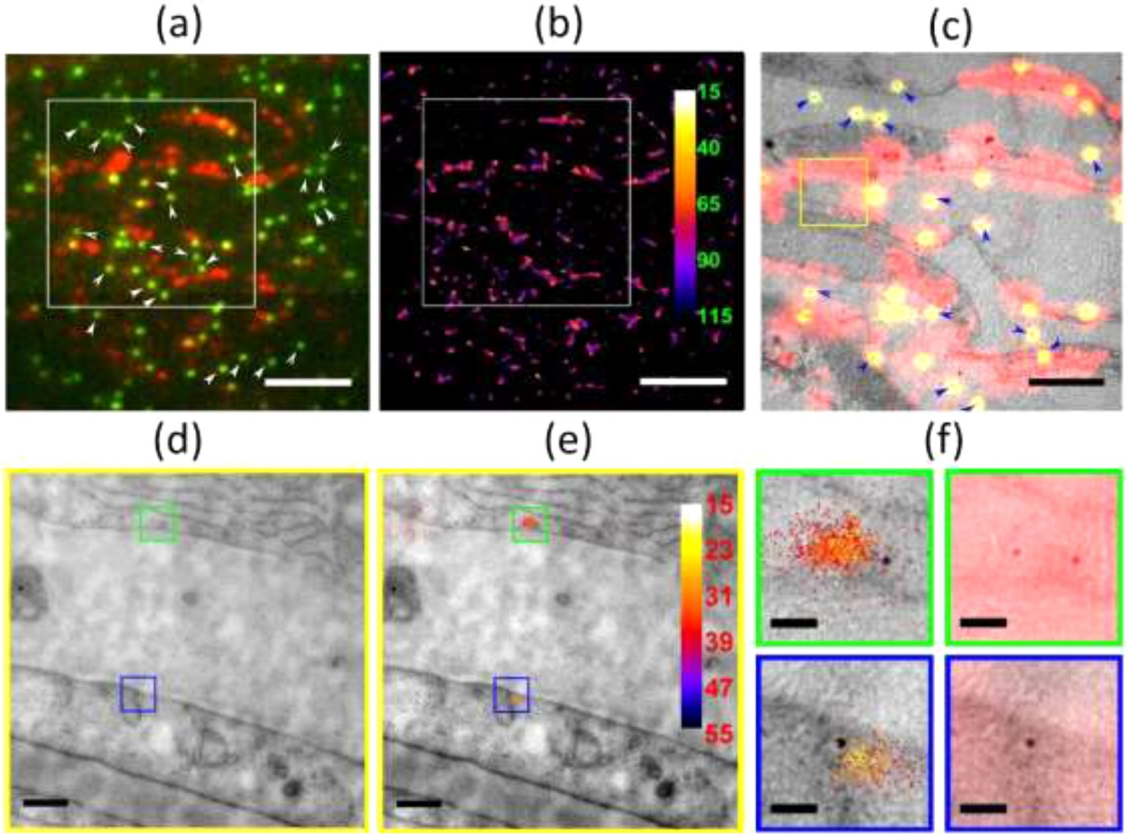

Fig. 6. SR-iCLEM of Caveolin. (a) Sum of the first 100 frames of the FM time series overlaid with an image of TetraSpeck fiducial markers. (b) Reconstructed SR image of the events in the FM time series. Color bar shows the uncertainty of the localization in nm. (c) Overlay of the fiducial image, Alexa Fluor®647 image and low magnification TEM image of the region indicated by the white square in (a) and (b). The blue arrows show the same fiducials indicated by the white arrows in (a). (d) High magnification TEM image from the area shown in yellow square in (c).. (e) Overlay of SR image with high magnification TEM image of the region indicated by the yellow square in (c). (f) Zoomed in image of the blue and green squares in (e) together with the same overlay done for normal fluorescence on the right. Scalebars: 10 μm for a and b, 5 μm for c, 500 nm for d and e and 100 nm for f.(For interpretation of the references to color in this figure legend, the reader is referred to the web version of this article.)

b. In this region, more than 25 TetraSpeck™ fiducial markers were visible in the TEM image (Fig. 6c, yellow spots with black dots). The white and blue arrowheads inside the white box of Fig. 6a and 6c respectively, correspond with the same fiducial markers. These fiducial markers were used to calculate the transformation matrix (T_{FL}) from the SR-FM to the low magnification TEM image. Fig. 6c also shows the overlay of the low magnification TEM image with the regular FM images in Fig. 6a using T_{FL}. We note that overlaying SR-FM with low magnification TEM images (Fig. S3 in SI) offers the possibility to identify regions with high localization accuracy that can be subsequently studied with high magnification TEM. Fig. 6d shows the high magnification TEM image of the area indicated by the yellow square in Fig. 6c.

By cross correlating the low and high magnification TEM images, T_{LH} was calculated. The total transformation matrix ($T_{tot} = T_{FL} \times T_{LH}$) was then applied on the drift corrected fluorescence image as well as the drift corrected SR image and overlaid with the high magnification TEM image (Fig. 6e). Here, only fluorescence events with localization uncertainty of 40 nm or better are shown. Fig. 6f shows two enlarged sections of the areas indicated by the blue and green squares in Fig. 6e. These typical examples reveal that the SR signal and the gold markers overlap within about 50 nm. This suggests that the gold label and the fluorescence originate from the same Caveola. The caveola themselves, however, are not always clearly visible. For comparison purposes, the same areas overlaid with normal fluorescence are also provided on the right.

3.3. Analysis of events

The overlay in Fig. 6f shows clear correlation between the presence of gold label and Alexa Fluor®647. In areas with both gold label and a signal in the Alexa Fluor®647 detection channel, we assumed that there is no signal from false positives. Such areas were used to analyze the statistics of the single molecule events. The singly dye events, 22500 in total, were analyzed by plotting histograms of the number of detected photons per event (N), the background standard deviation (b) and the localization uncertainty (σ) (Fig. 7). The intensity peaks around 265 photons (Fig. 7a) and the background standard deviation median is about 10 photons (Fig. 7b). Importantly, the localization uncertainty is found to peak at about 54 nm with a FWHM of 36 nm (Fig. 7c). This result is in accordance with the Fig. 2c which predicts a resolution of about 54 nm for 265 detected photons and a background standard deviation of 10 photons.

3.4. Overlay accuracy

In correlative microscopy, both the optical resolution and the overlay accuracy of the optical and EM images are of importance. The optical resolution is here determined by the localization uncertainty of the fluorophores and is given by Eq. 5. The overlay accuracy is, however, more difficult to predict. To assess the overlay accuracy of the SR-FM and high magnification TEM images, the errors in the positions of the fiducial markers in the same field in both modalities were calculated after the correlation procedure was carried out. By directly

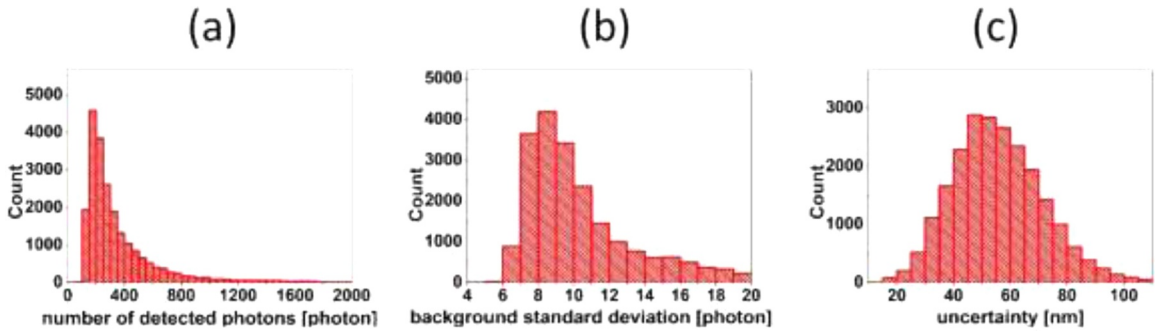

Fig. 7. Histograms of important localization parameters. (a) Number of photons per blinking event. (b) Background standard deviation of events in photons. (c) Localization uncertainty in nm.

comparing the centers of the positions of the fiducial markers in FM and TEM images a mean correlation accuracy of about 28 ± 11 nm was found (N = 27). This accuracy is well below the localization uncertainty.

4. Discussion and conclusion

In this work, a localization based super resolution fluorescence microscope is integrated inside a TEM column. The limited space between TEM poles and the vacuum environment in the column excludes using high *NA* (immersion) objectives. To realize acceptable localization uncertainty using a low *NA* objective requires use of bright fluorophores. In addition, the fluorophore should fluoresce and exhibit on/off switching under vacuum conditions. Here, Alexa Fluor®647 was used in combination with a Polystyrene supporting film. This resulted in a low background standard deviation levels of ~10 photons, reasonably high detected signal levels of ~265 photons and a localization uncertainty of 54 ± 18 nm. We note that not all specimens showed sufficient blinking for SR imaging. The reason for this is not clear, more research is required to identify the factors that affect the spontaneous blinking of Alexa Fluor®647 in vacuum and optimize its behavior.

Besides the localization uncertainty of the SR microscope, several other factors are of importance. Stage drift needs to be corrected for and the overlay of the fluorescence and high magnification TEM images need to be accurate. Both drift correction and accurate overlaying can be realized using fiducial markers. Here, TetraSpeck microspheres were used as fiducial markers. At the excitation wavelength of Alexa Fluor®647 their brightness was much lower than Alexa Fluor®647 during the recording of the FM time series.

After the recording of the FM time series, a series of images with only the signal from the TetraSpeck microspheres were recorded for accurate overlaying the reconstructed SR-FM image and the low magnification TEM image. They were also used for calculating the overlay accuracy of SR-FM and high magnification TEM images (28 nm). Together with the localization uncertainty of 54 nm, the total accuracy of mapping the center of an event in the localization series on top of the high magnification TEM image is about 61 nm ($\sqrt{54^2 + 28^2} = 61$). High overlay accuracies are more often realized in CLEM [43-45]. This enables accurate mapping of the fluorescence signal onto the high magnification TEM image. The TetraSpeck™ microspheres used in this work were significantly dimmer than the Alexa Fluor®647 in FM time series, making it difficult to distinguish them from labels. In addition, they were not always easy to find back in the low magnification TEM images. Previously, fiducial markers based on fluorescently labeled silica coated gold nanoparticles [46] were developed in our group. Their main advantages are the high brightness in FM and the excellent visibility of the 15 nm gold core in low magnification TEM. The presence of the gold core allows determination of the center of the fiducial markers with an accuracy of better than 15 nm. These particles have not been used here.

In combination with the high accuracy overlay method used here, regions for high magnification TEM can be easily selected. The overlay procedure relies on visibility of the same fiducial markers in FM and low magnification TEM and offers prospects of automatic overlaying of SR-FM and low magnification TEM images. Based on this overlay, regions can be selected for further examination with high magnification TEM. Since identification of the ROI is done using low magnification TEM, the specimen is exposed to only a low electron dose. This reduces distortion and damage of the specimen by the electron beam and is advantageous in many applications including (cryo-)tomography.

Localization based SR microscopy is usually slow since the single molecule events are temporally separated, and each frame needs to have only a sparse subset of blinking fluorophores. Short SR-FM measurement times are advantageous. Stage drift increases with time and the number of events with high localization accuracy decreases in time (Fig. S4 in SI). Here, SR-FM measurement times were 8–10 min. This can be reduced by increasing laser power and reducing the camera exposure time.

Integration of a (SR-)FM into a TEM can speed up the correlative measurement procedure and helps to avoid possible damage and deterioration of the specimen due to transfer of the specimen between two machines. However, the sample preparation for the integrated approach can be cumbersome. The heavy metals used for producing (membrane) contrast in the TEM quench the fluorescence signal. Therefore, the sample preparation procedure needs to balance ultrastructure visibility and preservation of fluorescence. We also note that not all fluorophores emit light under dry vacuum condition and even fewer are suitable for SR-FM.

The use of the same sample stage for FM and TEM in our integrated CLEM system offers a simple and fast way of finding back regions of interest. After identifying a ROI in fluorescence mode, finding it back in TEM only involves rotating and translating the TEM sample holder followed by recoding a TEM image. The relation between the coordinates in the fluorescence and TEM images is linear which makes it straightforward to find back the ROI; the accuracy of this step is already within 1 μm and the time required to switch imaging modes is only a few seconds. The reliability and ease of finding back ROI's in this approach has been extensively demonstrated in previous work [5,9,11,47,48].

In the case of wide-field and confocal FM, the optical resolution is far worse than the overlay accuracy and therefore the information content of the overlay is limited by the resolution of the FM. Fluorescent spots with the size of the diffraction limit, hundreds of nm's, may contain multiple labeled structures that cannot be distinguished. This can introduce ambiguities that complicate the correlation process and hides valuable information. The addition of SR to CLEM mitigates this problem and enables high correlation accuracy (here ~28 nm) in combination with high optical resolution (here ~50 nm), such that even closely separated structures can be mapped onto the TEM image. Importantly, localization based SR techniques rely on the capability of FM to detect the signal of single fluorescent molecules. In combination

with CLEM this opens up the possibility to map the signal of, for instance, a single protein labeled with a single dye molecule onto the TEM image. This offers the prospect of imaging the local ultrastructure in the vicinity of a fluorescently labeled protein without the use of gold labels, albeit with a correlation accuracy of several tens of nm. Here, the viability of this approach was demonstrated using fluorescently and gold labeled Caveola. Distortions of the specimen are a serious threat and need to be avoided as much as possible. Here, integrated CLEM has clear advantages since no transfer between different instruments is required.

Live cell SR-FM is still in its infancy due to limitations of the different SR-FM techniques [49–53]. Complications include phototoxicity due to high laser intensities in the case of, e.g., STED [54,55] and acquisition speed in the case of localization based techniques [15]. Once these issues have been solved a live cell integrated correlative imaging workflow may be feasible when microfluidic systems are used [56].

The experiments reported in this work were carried out on Lowicryl sections. The Lowicryl sections were labeled with primary antibody and PAG and next the section was labeled with the fluorescent dye. In this way, the fluorescent dyes on top of the section are comparatively far away from the heavy metals in the section and quenching of the fluorescence is prevented. Integrated CLEM approaches will benefit from new developments in, for instance, (fixation-resistant) fluorescent proteins [57] as well as novel preparation methods .

Here, no extensive research on the best fluorescent dye for SR imaging under vacuum conditions was performed. Alexa Fluor®647 was found to spontaneous blink under dry vacuum conditions, which made it easy to use in localization-based SR microscopy. No optimization of the labeling conditions was attempted; doing so could result in brighter signals and improved blinking behavior. Caged dyes may be promising for use in integrated CLEM systems since they usually do not require the use of special buffers. This type of dye offers the prospect of controlling the number of simultaneously active fluorophores in a region.

The integrated SR CLEM system presented here can only operate at room temperature. Integrated SR CLEM will be even more valuable for imaging under cryo conditions; when separate setups are used, contamination can be easily picked up during the transfer between the setups [5]. Moreover, this would also avoid the use of heavy metals that quench fluorescence.

Although the TEM destroys fluorescence from commonly used fluorophores, there are prospects of carrying out experiments involving time correlation in the integrated setup. The switching between fluorescence and TEM mode in the integrated setup only takes seconds. When an in-situ TEM holder is used, a process can be followed in time in fluorescence mode and after switching to TEM mode studied in high resolution. Possible application would be, e.g., studies on mineralization of collagen [58] and photon/e-beam induced lithography using liquid precursors in in-situ TEM holders [59]. The SR CLEM setup described in this work is also interesting for other studies in material sciences. Previously we demonstrated its use in a study on the activity of catalysts [60].

Declaration of Competing Interest

The authors declare that they have no competing interests.

Acknowledgments

This work is part of the Microscopy Valley programme project number 12713, financed by the Netherlands Organisation for Scientific Research (NWO). The authors thank Maarten Tuijtel for making the photograph of the objective mounted on the TEM octagon.

Supplementary materials

Supplementary material associated with this article can be found, in the online version, at doi:10.1016/j.ultramic.2020.113007.

Reference

[1] T. Ando, et al., The 2018 correlative microscopy techniques roadmap, J. Phys. D Appl. Phys. 51 (44) (2018) 443001.
[2] F.J. Timmermans, C. Otto, Contributed review: review of integrated correlative light and electron microscopy, Rev. Sci. Instrum. 86 (1) (2015) 011501.
[3] P. De Boer, J.P. Hoogenboom, B.N. Giepmans, Correlated light and electron microscopy: ultrastructure lights up!, Nat. Methods 12 (6) (2015) 503–513.
[4] C.L. Fonta, B.M. Humbel, Correlative microscopy, Arch. Biochem. Biophys. 581 (2015) 98–110.
[5] F.G.A. Faas, et al., Localization of fluorescently labeled structures in frozen-hydrated samples using integrated light electron microscopy, J. Struct. Biol. 181 (3) (2013) 283–290.
[6] M.A. Karreman, et al., Optimizing immuno-labeling for correlative fluorescence and electron microscopy on a single specimen, J. Struct. Biol. 180 (2) (2012) 382–386.
[7] C.J. Peddie, N. Liv, J.P. Hoogenboom, L.M. Collinson, Integrated light and scanning electron microscopy of GFP-expressing cells, Methods Cell Biol. 124 (2014) 363–389.
[8] M.A. Karreman, E.G. Van Donselaar, A.V. Agronskaia, C.T. Verrips, H.C. Gerritsen, Novel contrasting and labeling procedures for correlative microscopy of thawed cryosections, J. Histochem. Cytochem. 61 (3) (2013) 236–247.
[9] M.A. Karreman, A.V. Agronskaia, A.J. Verkleij, F.F. Cremers, H.C. Gerritsen, B.M. Humbel, Discovery of a new RNA-containing nuclear structure in UVC-induced apoptotic cells by integrated laser electron microscopy, Biol. Cell 101 (5) (2009) 287–299.
[10] N. Liv, et al., Simultaneous correlative scanning electron and high-NA fluorescence microscopy, PLoS One 8 (2) (2013) e55707.
[11] A.V. Agronskaia, et al., Integrated fluorescence and transmission electron microscopy, J. Struct. Biol. 164 (2) (2008) 183–189.
[12] H. Iijima, Y. Fukuda, Y. Arai, S. Terakawa, N. Yamamoto, K. Nagayama, Hybrid fluorescence and electron cryo-microscopy for simultaneous electron and photon imaging, J. Struct. Biol. 185 (1) (2014) 107–115.
[13] I. Solomonov, D. Talmi-Frank, Y. Milstein, S. Addadi, A. Aloshin, I. Sagi, Introduction of correlative light and airSEMTM microscopy imaging for tissue research under ambient conditions, Sci. Rep. 4 (2014).
[14] A.C. Zonnevylle, et al., Integration of a high-NA light microscope in a scanning electron microscope, J. Microsc. 252 (1) (2013) 58–70.
[15] B. Huang, M. Bates, X. Zhuang, Super-resolution fluorescence microscopy, Annu. Rev. Biochem. 78 (2009) 993–1016.
[16] B.G. Kopek, G. Shtengel, J.B. Grimm, D.A. Clayton, H.F. Hess, Correlative photoactivated localization and scanning electron microscopy, PLoS One 8 (10) (2013) e77209.
[17] B.G. Kopek, G. Shtengel, C.S. Xu, D.A. Clayton, H.F. Hess, Correlative 3D super-resolution fluorescence and electron microscopy reveal the relationship of mitochondrial nucleoids to membranes, Proceedings of the National Academy of Sciences, 109 2012, pp. 6136–6141.
[18] S. Watanabe, et al., Nanometer-resolution fluorescence electron microscopy (nano-EM) in cultured cells, Electron Microscopy: Methods and Protocols, Springer, 2014, pp. 503–526.
[19] S. Watanabe, et al., Protein localization in electron micrographs using fluorescence nanoscopy, Nat. Methods 8 (1) (2011) 80–84.
[20] C.J. Peddie, et al., Correlative super-resolution fluorescence and electron microscopy using conventional fluorescent proteins in vacuo, J. Struct. Biol. (2017).
[21] S.W. Hell, J. Wichmann, Breaking the diffraction resolution limit by stimulated emission: stimulated-emission-depletion fluorescence microscopy, Opt. Lett. 19 (11) (1994) 780–782.
[22] M.G. Gustafsson, Nonlinear structured-illumination microscopy: wide-field fluorescence imaging with theoretically unlimited resolution, Proceedings of the National Academy of Sciences of the United States of America, 102 2005, pp. 13081–13086.
[23] M.G. Gustafsson, Surpassing the lateral resolution limit by a factor of two using structured illumination microscopy, J. Microsc. 198 (2) (2000) 82–87.
[24] R. Heintzmann, C. Cremer, Laterally modulated excitation microscopy: improvement of resolution by using a diffraction grating, *Proceedings Of SPIE*, 3568 1999, p. 15.
[25] P. Tinnefeld, C. Eggeling, S.W. Hell, Far-Field Optical Nanoscopy 14 Springer, 2015.
[26] M.J. Rust, M. Bates, X. Zhuang, Sub-diffraction-limit imaging by stochastic optical reconstruction microscopy (STORM), Nat. Methods 3 (10) (2006) 793–796.
[27] M. Heilemann, et al., Subdiffraction-resolution fluorescence imaging with conventional fluorescent probes, Angew. Chem. Int. Ed. 47 (33) (2008) 6172–6176.
[28] J. Fölling, et al., Fluorescence nanoscopy by ground-state depletion and single-molecule return, Nat. Methods 5 (11) (2008) 943–945.
[29] M. Lampe, W. Fouquet, Requirements for samples in super-resolution fluorescence microscopy, Super-Resolution Microscopy Techniques in the Neurosciences, Springer, 2014, pp. 343–367.
[30] E. Betzig, et al., Imaging intracellular fluorescent proteins at nanometer resolution, Science 313 (5793) (2006) 1642–1645.
[31] S.T. Hess, T.P. Girirajan, M.D. Mason, Ultra-high resolution imaging by fluorescence photoactivation localization microscopy, Biophys. J. 91 (11) (2006) 4258–4272.

[32] G.T. Dempsey, J.C. Vaughan, K.H. Chen, M. Bates, X. Zhuang, Evaluation of fluorophores for optimal performance in localization-based super-resolution imaging, Nat. Methods 8 (12) (2011) 1027.
[33] L. Nahidiazar, A.V. Agronskaia, J. Broertjes, B. van den Broek, K. Jalink, Optimizing imaging conditions for demanding multi-color super resolution localization microscopy, PLoS One 11 (7) (2016) e0158884.
[34] B. Zhang, J. Zerubia, J.-C. Olivo-Marin, Gaussian approximations of fluorescence microscope point-spread function models, Appl. Opt. 46 (10) (2007) 1819–1829.
[35] S. Stallinga, B. Rieger, The effect of background on localization uncertainty in single emitter imaging, Biomedical Imaging (ISBI), 2012 9th IEEE International Symposium on, 2012, pp. 988–991.
[36] M.D. Benoy, E.M. Mohammed, M. Suresh Babu, P.J. Binu, B. Pradeep, Thickness dependence of the properties of indium tin oxide (ITO) films prepared by activated reactive evaporation, Braz. J. Phys. 39 (4) (2009) 629–632.
[37] M. Mazur, D. Kaczmarek, J. Domaradzki, D. Wojcieszak, S. Song, F. Placido, Influence of thickness on transparency and sheet resistance of ITO thin films, Advanced Semiconductor Devices & Microsystems (ASDAM), 2010 8th International Conference on, 2010, pp. 65–68.
[38] B. Valeur, Effects of intermolecular photophysical processes on fluorescence emission, Molecular Fluorescence: Principles and Applications, Wiley, 2001, pp. 72–124.
[39] M.A. Hayat, Principles and Techniques of Electron Microscopy: Biological Applications, 4th ed., Cambridge University Press, 2000.
[40] M. A. Karreman, *Lights will guide you: sample preparation and applications for integrated laser and electron microscopy*. 2013.
[41] M. Ovesnỳ, P. Křížek, J. Borkovec, Z. Švindrych, G.M. Hagen, ThunderSTORM: a comprehensive ImageJ plug-in for PALM and STORM data analysis and super-resolution imaging, Bioinformatics 30 (16) (2014) 2389–2390.
[42] S. Mohammadian, et al., High accuracy, fiducial marker-based image registration of correlative microscopy images, Sci. Rep. 9 (1) (Mar. 2019) 3211.
[43] M.T. Haring, et al., Automated sub-5 nm image registration in integrated correlative fluorescence and electron microscopy using cathodoluminescence pointers, Sci. Rep. 7 (2017).
[44] M.W. Tuijtel, et al., Inducing fluorescence of uranyl acetate as a dual-purpose contrast agent for correlative light-electron microscopy with nanometre precision, Sci. Rep. 7 (2017).
[45] W. Kukulski, M. Schorb, S. Welsch, A. Picco, M. Kaksonen, J.A. Briggs, Precise, correlated fluorescence microscopy and electron tomography of lowicryl sections using fluorescent fiducial markers, Methods Cell. Biol. 111 (2012) 235–257.
[46] J. Fokkema, et al., Fluorescently labelled silica coated gold nanoparticles as fiducial markers for correlative light and electron microscopy, Sci. Rep. 8 (2018) 13625.
[47] M.A. Karreman, I.L. Buurmans, A.V. Agronskaia, J.W. Geus, H.C. Gerritsen, B.M. Weckhuysen, Probing the different life stages of a fluid catalytic cracking particle with integrated laser and electron microscopy, Chem.-A Eur. J. 19 (12) (2013) 3846–3859.
[48] M.A. Karreman, et al., Integrated laser and electron microscopy correlates structure of fluid catalytic cracking particles to Brønsted acidity, Angew. Chem. Int. Ed. 51 (6) (2012) 1428–1431.
[49] F. Bottanelli, et al., Two-colour live-cell nanoscale imaging of intracellular targets, Nat. Commun. 7 (2016) 10778.
[50] S.A. Jones, S.-H. Shim, J. He, X. Zhuang, Fast, three-dimensional super-resolution imaging of live cells, Nat. Methods 8 (6) (2011) 499.
[51] G. Lukinavičius, et al., Fluorogenic probes for live-cell imaging of the cytoskeleton, Nat. Methods 11 (7) (2014) 731.
[52] G.C. Mo, et al., Genetically encoded biosensors for visualizing live-cell biochemical activity at super-resolution, Nat. Methods 14 (4) (2017) 427.
[53] M. Ratz, I. Testa, S.W. Hell, S. Jakobs, CRISPR/Cas9-mediated endogenous protein tagging for RESOLFT super-resolution microscopy of living human cells, Sci. Rep. 5 (2015) 9592.
[54] S.J. Sahl, S.W. Hell, S. Jakobs, Fluorescence nanoscopy in cell biology, Nat. Rev. Mol. Cell Biol. 18 (11) (2017) 685.
[55] M.B. Stone, S.A. Shelby, S.L. Veatch, Super-Resolution microscopy: shedding light on the cellular plasma membrane, Chem. Rev. (2017).
[56] E.A. Ring, N. De Jonge, Microfluidic system for transmission electron microscopy, Microsc. Microanal. 16 (5) (2010) 622–629.
[57] M.G. Paez-Segala, et al., Fixation-resistant photoactivatable fluorescent proteins for CLEM, Nat. Methods 12 (3) (2015) 215–218.
[58] X. Wang, J. Yang, C.M. Andrei, L. Soleymani, K. Grandfield, Biomineralization of calcium phosphate revealed by in situ liquid-phase electron microscopy, Commun. Chem. 1 (1) (2018) 80.
[59] M.W. van de Put, C.C. Carcouët, P.H. Bomans, H. Friedrich, N. de Jonge, N.A. Sommerdijk, Writing silica structures in liquid with scanning transmission electron microscopy, Small 11 (5) (2015) 585–590.
[60] F.C. Hendriks, et al., Integrated transmission electron and single-molecule fluorescence microscopy correlates reactivity with ultrastructure in a single catalyst particle, Angew. Chem. 130 (1) (2018) 263–267.